How Much More Rain Will Global Warming Bring?
Frank J. Wentz, *et al.*
Science **317**, 233 (2007);
DOI: 10.1126/science.1140746

Science (print ISSN 0036-8075; online ISSN 1095-9203) is published weekly, except the last week in December, by the American Association for the Advancement of Science, 1200 New York Avenue NW, Washington, DC 20005.

15. T. Kunihiro, K. Nagashima, H. Yurimoto, *Geochim. Cosmochim. Acta* **69**, 763 (2005).
16. Materials and methods are available as supporting material on *Science* Online.
17. K. Nagashima, A. N. Krot, H. Yurimoto, *Nature* **428**, 921 (2004).
18. E. D. Young, S. S. Russell, *Science* **282**, 452 (1998).
19. $\delta^{i}O_{SMOW}$ (‰) ≡ $[(^{i}O/^{16}O)_{sample}/(^{i}O/^{16}O)_{SMOW} - 1] \times 1000$, where $i = 17$ or 18.
20. T. R. Ireland, P. Holden, M. D. Norman, J. Clarke, *Nature* **440**, 776 (2006).
21. L. H. Fuchs, E. Olsen, K. J. Jensen, *Smithson. Contrib. Earth Sci.* **10**, 1 (1973).
22. K. Tomeoka, P. R. Buseck, *Geochim. Cosmochim. Acta* **49**, 2149 (1985).
23. B. Fegley Jr., *Space Sci. Rev.* **92**, 177 (2000).
24. D. S. Lauretta, D. T. Kremser, B. Fegley Jr., *Icarus* **122**, 288 (1996).
25. Y. Hong, B. Fegley Jr., *Meteorit. Planet. Sci.* **33**, 1101 (1997).
26. R. N. Clayton, T. K. Mayeda, *Geochim. Cosmochim. Acta* **63**, 2089 (1999).
27. A. Greshake, *Geochim. Cosmochim. Acta* **61**, 437 (1997).
28. E. D. Young, *Philos. Trans. R. Soc. London A* **359**, 2095 (2001).
29. B.-G. Choi, K. D. McKeegan, A. N. Krot, J. T. Wasson, *Nature* **392**, 577 (1998).
30. A. N. Krot, B. Fegley Jr., K. Lodders, H. Palme, in *Protostars and Planets IV*, V. Mannings, A. P. Boss, S. S. Russell, Eds. (Univ. of Arizona Press, Tucson, AZ, 2000) pp. 1019–1054.
31. J. M. W. Chase, *NIST-JANAF Thermochemical Tables, Fourth edition, Journal of Physical and Chemical Reference Data, Monograph 9, Parts I and II* (American Institute of Physics, New York, 1998).
32. We thank Y. Matsuhisa for providing a magnetite standard, T. Kaito and I. Nakatani for assistance with focused ion beam sample preparation, K. Tomeoka for indicating Murchison tochilinite, and E. D. Scott and G. R. Huss for discussion. This work was partly supported by Monkasho (H.Y.) and NASA (A.N.K.).

Supporting Online Material

www.sciencemag.org/cgi/content/full/1142021/DC1
Materials and Methods
Fig. S1
Tables S1 and S2
References

2 March 2007; accepted 17 May 2007
Published online 14 June 2007;
10.1126/science.1142021
Include this information when citing this paper.

How Much More Rain Will Global Warming Bring?

Frank J. Wentz,* Lucrezia Ricciardulli, Kyle Hilburn, Carl Mears

Climate models and satellite observations both indicate that the total amount of water in the atmosphere will increase at a rate of 7% per kelvin of surface warming. However, the climate models predict that global precipitation will increase at a much slower rate of 1 to 3% per kelvin. A recent analysis of satellite observations does not support this prediction of a muted response of precipitation to global warming. Rather, the observations suggest that precipitation and total atmospheric water have increased at about the same rate over the past two decades.

In addition to warming Earth's surface and lower troposphere, the increase in greenhouse gas (GHG) concentrations is likely to alter the planet's hydrologic cycle (*1*–*3*). If the changes in the intensity and spatial distribution of rainfall are substantial, they may pose one of the most serious risks associated with climate change. The response of the hydrologic cycle to global warming depends to a large degree on the way in which the enhanced GHGs alter the radiation balance in the troposphere. As GHG concentrations increase, the climate models predict an enhanced radiative cooling that is balanced by an increase in latent heat from precipitation (*1*, *2*). The Coupled Model Intercomparison Project (*4*) and similar modeling analyses (*1*–*3*) predict a relatively small increase in precipitation (and likewise in evaporation) at a rate of about 1 to 3% K^{-1} of surface warming. In contrast, both climate models and observations indicate that the total water vapor in the atmosphere increases by about 7% K^{-1} (*1*–*3*, *5*, *6*).

More than 99% of the total moisture in the atmosphere is in the form of water vapor. The large increase in water is due to the warmer air being able to hold more water vapor, as dictated by the Clausius-Clapeyron (C-C) relation under the condition that the relative humidity in the lower troposphere stays constant. So according to the current set of global coupled ocean-atmosphere models (GCMs), the rate of increase in precipitation will be several times lower than that for total water. This apparent inconsistency is resolved in the models by a reduction in the vapor mass flux, particularly with respect to the Walker circulation, which reinforces the trade winds (*3*, *7*). Whether a decrease in global winds is a necessary consequence of global warming is a complex question that is yet to be resolved (*8*).

Using satellite observations from the Special Sensor Microwave Imager (SSM/I), we assessed the GCMs' prediction of a muted response of rainfall and evaporation to global warming. The SSM/I is well suited for studying the global hydrologic cycle in that it simultaneously measures precipitation (P), total water vapor (V), and also surface-wind stress (τ_0), which is the principal term in the computation of evaporation (E) (*8*, *9*).

The SSM/I data set extends from 1987 to 2006. During this time Earth's surface temperature warmed by 0.19 ± 0.04 K $decade^{-1}$, according to the Global Historical Climatology Network (*10*, *11*). Satellite measurements of the lower troposphere show a similar warming of 0.20 ± 0.10 K $decade^{-1}$ (*12*). The error bars are at the 95% confidence level. This warming is consistent with 20th-century climate-model runs (*13*) and provides a reasonable, albeit short, test bed for assessing the impact of global warming on the hydrologic cycle.

When averaged globally over monthly time scales, P and E must balance except for a negligibly small storage term. This $E = P$ constraint provides a useful consistency check with which to evaluate our results. However, the constraint is valid only for global averages. Accordingly, the first step in our analysis was to construct global monthly maps of P and E at a 2.5° spatial resolution for the period 1987 to 2006.

The SSM/I retrievals used here are available only over the ocean. To supplement the SSM/I over-ocean rain retrievals, we used the land values from the Global Precipitation Climatology Project data set, which is a blend of satellite retrievals and rain gauge measurements (*14, 15*). Satellite rain retrievals over land were less accurate than their ocean counterparts, but this drawback was compensated by the fact that there are abundant rain gauges over land for constraining the satellite retrievals. Likewise, global evaporation was computed separately for oceans and land. Because 86% of the world's evaporation comes from the oceans (*16*), ocean evaporation was our primary focus. We computed evaporation over the oceans with the use of the bulk formula from the National Center for Atmospheric Research Community Atmospheric Model 3.0 (*8*, *17*). Evaporation over land cannot be derived from satellite observations, and we resorted to using a constant value of 527 mm $year^{-1}$ for all of the continents, excluding Antarctica (*16*). For Antarctica and sea ice, we used a value of 28 mm $year^{-1}$ (*8*, *16*).

The GCMs indicate that E should increase about 1 to 3% K^{-1} of surface warming. However, according to the bulk formula (eq. S1) (*8*), evaporation increases similarly to C-C as the surface temperature warms, assuming that the other terms remain constant. For example, a global increase of 1 K in the surface air temperature produces a 5.7% increase in E (*8*). To obtain the muted response of 1 to 3% K^{-1}, other variables in the bulk formula need to change with time. The air-sea temperature difference and the near-surface relative humidity are expected to remain nearly constant (*8*), and this leaves τ_0 as the one variable that can reduce evaporation to the magnitude required to balance the radiation budget in the models. To bring the bulk formula into agreement with the radiative cooling constraint, $\sqrt{\tau_0}$

Remote Sensing Systems, 438 First Street, Santa Rosa, CA 95401, USA.

*To whom correspondence should be addressed. E-mail: frank.wentz@remss.com

would need to decrease by about 4% K^{-1}. Thus, a muted response of precipitation to global warming requires a decrease in global winds (*2*, *3*, *7*).

To evaluate the GCMs' prediction of a decrease in winds, we looked at the 19 years of SSM/I wind retrievals. These winds are expressed in terms of an equivalent neutral-stability wind speed (W) at a 10-m elevation, which is proportional to $\sqrt{\tau_0}$ (*8*, *16*). Figure 1 shows a decadal trend map of W. For each 2.5° grid cell, a least-squares linear fit to the 19-year time series was calculated after removing the seasonal variability. The wind trends from the International Comprehensive Ocean-Atmosphere Data Set (ICOADS) are also shown, but just for comparison. They were not used in our analysis. Although the ICOADS trend map is very noisy because of sampling and measurement deficiencies, it shows trends similar to those from the SSM/I in the northern Atlantic and Pacific, where the ICOADS ship observations are more abundant. The North Atlantic Oscillation (NAO) is apparent in both trend maps as a tripole feature with increasing winds between 30°N and 40°N and decreasing winds to the north and south (*18*). This feature is consistent with the observed decrease in the NAO index since 1987. When averaged over the tropics from 30°S to 30°N, the winds increased by 0.04 m s^{-1} (0.6%) $decade^{-1}$, and over all oceans the increase was 0.08 m s^{-1} (1.0%) $decade^{-1}$. The SSM/I wind retrievals were validated by comparisons with moored ocean buoys and satellite scatterometer wind retrievals (fig. S1). On the basis of this analysis, the error bar on the SSM/I wind trend is estimated to be ±0.05 m s^{-1} $decade^{-1}$ at the 95% confidence level (*8*). This observed increase in the SSM/I winds is opposite to the GCM results, which predict that the 1987-to-2006 warming should have been accompanied by a decrease in winds on the order of (0.19 K $decade^{-1}$)(4% K^{-1}) = 0.8% $decade^{-1}$.

We then looked at the variability of global precipitation and evaporation during the past two decades. Figure 2A shows the time series for P and E. Also shown is the over-ocean SSM/I retrieval of V. To generate the time series, the seasonal variability was first removed, and then the variables were low-pass filtered by convolution with a Gaussian distribution that had a ±4-month width at half-peak power. The major features apparent in the time series are the 1997–1998 El Niño and the 1986–1987 El Niño, followed by the strong 1988–1989 La Niña. It is noteworthy that E, P, and V all exhibited similar magnitudes for interannual variability and decadal trends (Table 1). After applying the ±4-month smoothing, the correlation of E versus P was 0.68. Because global precipitation and evaporation must balance, the observed differences in the derived values of P and E provided an error estimate that we used to estimate the uncertainty in the decadal trend. The estimated error bar at the 95% confidence level for E and P is ±0.5% $decade^{-1}$ (*8*).

Also shown in Fig. 2A is the ensemble mean of nine climate-model simulations smoothed in

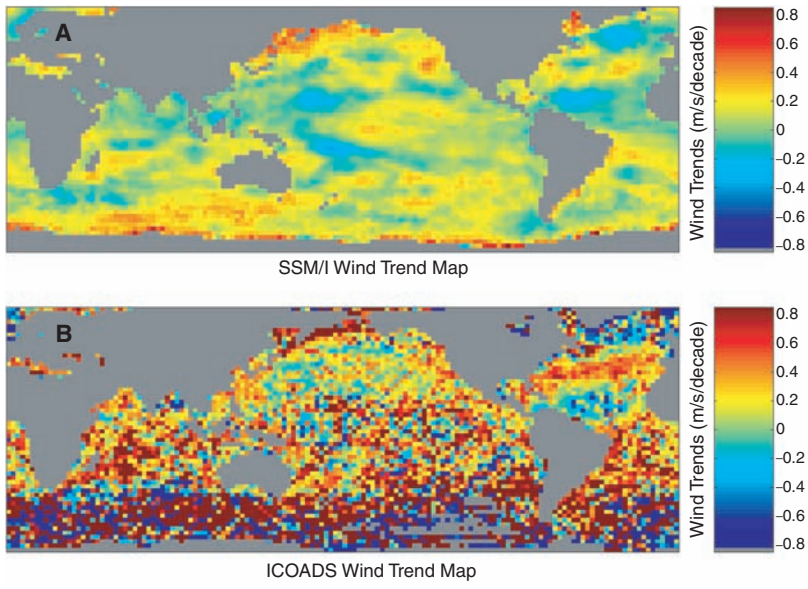

Fig. 1. Surface-wind trends for the period July 1987 through August 2006 computed at a spatial resolution of 2.5°. (**A**) SSM/I wind trends. (**B**) ICOADS wind trends. In the North Pacific and North Atlantic where ICOADS ship observations are more abundant, the two data sets show similar trends. The tripole feature in the North Atlantic is consistent with the recent decrease in the NAO index.

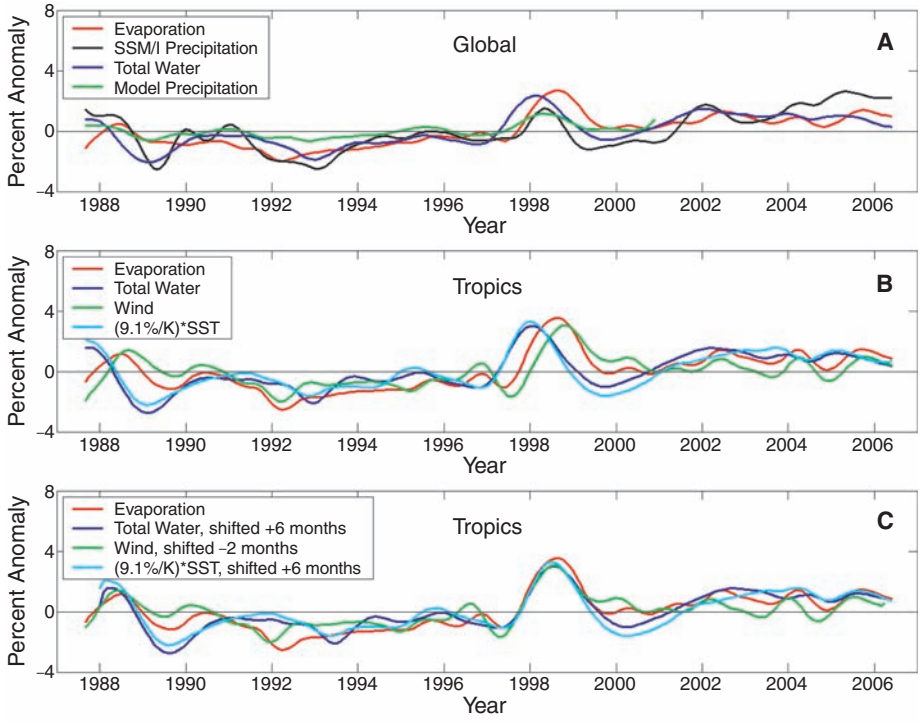

Fig. 2. Anomaly time series of the hydrologic variables. (**A**) Global results for the observed precipitation and evaporation and over-ocean results for total water vapor. The average model precipitation predicted by AMIP simulations is also shown. (**B**) Tropical ocean results for evaporation, total water vapor, surface-wind speed, and SST. The SST time series has been scaled by 9.1% K^{-1}. During the El Niños, evaporation and wind were not in phase with vapor and SST. At the end of 1996, SST and vapor began to increase while the winds began to decrease, with no net effect on evaporation. About 8 months later (mid-1997), the winds in the tropics began to recover and then increased sharply, reaching a maximum value in late 1998. All four variables remained at elevated values thereafter. (**C**) Same as (B), except that the water vapor and SST curves have been shifted forward in time by 6 months, and the wind curve has been shifted backward by 2 months. The statistics on the global time series, including error bars, are given in Table 1.

the same way as in the satellite observations. These climate runs, for which the sea-surface temperature (SST) is prescribed from observations, are from the Atmospheric Model Intercomparison Project II (AMIP-II) (*19, 20*). There is a pronounced difference between the precipitation time series from the climate models and that from the satellite observations. The amplitude of the interannual variability, the response to the El Niños, and the decadal trends are all smaller by a factor of 2 to 3 in the climate-model results, as compared with the observations. This characteristic of the models to underpredict the amplitude of precipitation changes to El Niño–Southern Oscillation events has been reported previously (*21*), and the results presented here suggest that the climate models are also underestimating the decadal variability.

The similarity in the satellite-derived time series became more pronounced when the analysis was limited to the tropical oceans (30°S to 30°N), where most of the evaporation occurs. Although the condition $E = P$ was no longer valid for this regional analysis, the coupling of evaporation with the other variables was more apparent. Figure 2B shows the tropical time series of *E*, *V*, *SST*, and *W*. The variables *V* and *SST* exhibited a high correlation [correlation coefficient (r) = 0.96], and their scaling relation of 9.1% K^{-1} was equal to the C-C rate (6.5% K^{-1}) times a moist adiabatic lapse rate (MALR) factor of 1.4 (*5*). The MALR factor is the ratio of change in the lower tropospheric temperature to the change in *SST*. This strong coupling between *V* and *SST* is another confirmation that the total atmospheric water increases with temperature at the C-C rate.

During the two El Niños, evaporation and wind speed were not in phase with vapor and *SST*. The increase in evaporation lagged the increase in vapor by 6 months, and the increase in winds lagged by 8 months (Fig. 2B). When a 6-month lag was applied, the correlation between *E* and *V* was 0.84 in the tropics and 0.88 globally.

Figure 3 shows a trend map of $P - E$. The most striking feature is in the tropical Western Pacific Warm Pool, where $\Delta(P - E)$ is about 400 mm $year^{-1}$ $decade^{-1}$, and Δ represents change. This is a region of maximum $P - E$ (1500 to 2000 mm $year^{-1}$). Simple hydrologic models predict that $\Delta(P - E)$ should vary similarly to $P - E$ (*3*). That is to say, wet regions should get wetter and dry regions should get drier. This seems to be the case over the Warm Pool, but elsewhere this direct proportionality is not as apparent.

During the past two decades, the hydrologic parameters *E*, *P*, and *V* exhibited similar responses to the two El Niños (apart from a 6-month lag), similar magnitudes of interannual variability (1.0 to 1.3%), and similar decadal trends (1.2 to 1.4% $decade^{-1}$). Earth's surface warmed by 0.2 K $decade^{-1}$ during this period, and hence the observed changes in *E* and *P* suggest an acceleration in the hydrologic cycle of about 6% K^{-1}, close to the C-C value. In addition, ocean winds exhibited a small increase of 1.0% $decade^{-1}$. There is no evidence in the observations that radiative forcing in the troposphere is inhibiting the variations in *E*, *P*, and *W*. Rather, *E* and *P* seem to simply vary in unison with the total atmospheric water content.

The reason for the discrepancy between the observational data and the GCMs is not clear. One possible explanation is that two decades is too short of a time period, and thus we see internal climate variability that masks the limiting effects of radiative forcing. However, we would argue that although two decades may be too short for extrapolating trends, it may indeed be long enough to indicate that the observed scaling relations will continue on a longer time scale. Another possible explanation is that there are errors in the satellite retrievals, but the consistency among the independent retrievals and validation of the winds with other data sets suggests otherwise. Lastly, there is the possibility that the climate models have in common a compensating error in characterizing the radiative balance for the troposphere and Earth's surface. For example, variations in modeling cloud radiative forcing at the surface can have a relatively large effect on the precipitation response (*4*), whereas the temperature response is more driven by how clouds affect the radiation at the top of the troposphere.

The difference between a subdued increase in rainfall and a C-C increase has enormous impact, with respect to the consequences of global warming. Can the total water in the atmosphere increase by 15% with CO_2 doubling but precipitation only increase by 4% (*1*)? Will warming really bring a decrease in global winds? The observations reported here suggest otherwise, but clearly these questions are far from being settled.

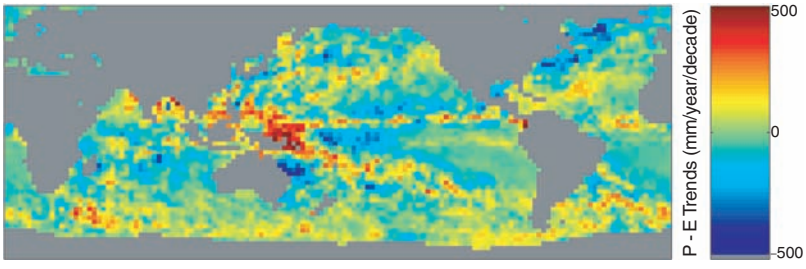

Fig. 3. Trends in satellite-derived $P - E$ for the period July 1987 through August 2006. The largest change was over the warm pool in the western Pacific: a wet area that became wetter.

Table 1. Statistics on the variation of global evaporation, global precipitation, and over-ocean water vapor for the period July 1987 through August 2006. The error bars on the trends are given at the 95% confidence level. The values in parentheses are in terms of percentage change, rather than absolute change.

Parameter	Mean	Standard deviation	Trend
Evaporation	961 mm $year^{-1}$	10.1 mm $year^{-1}$ (1.1%)	12.6 ± 4.8 mm $year^{-1}$ $decade^{-1}$ (1.3 ± 0.5% $decade^{-1}$)
Precipitation	950 mm $year^{-1}$	12.7 mm $year^{-1}$ (1.3%)	13.2 ± 4.8 mm $year^{-1}$ $decade^{-1}$ (1.4 ± 0.5% $decade^{-1}$)
Total water	28.5 mm	0.292 mm (1.0%)	0.354 ± 0.114 mm $decade^{-1}$ (1.2 ± 0.4% $decade^{-1}$)

References and Notes

1. M. R. Allen, W. J. Ingram, *Nature* **419**, 224 (2002).
2. J. F. B. Mitchell, C. A. Wilson, W. M. Cunnington, *Q. J. R. Meteorol. Soc.* **113**, 293 (1987).
3. I. M. Held, B. J. Soden, *J. Clim.* **19**, 5686 (2006).
4. C. Covey *et al.*, *Global Planet. Change* **37**, 103 (2003).
5. F. J. Wentz, M. Schabel, *Nature* **403**, 414 (2000).
6. K. E. Trenberth, J. Fasullo, L. Smith, *Clim. Dyn.* **24**, 741 (2005).
7. G. A. Vecchi *et al.*, *Nature* **441**, 73 (2006).
8. See supporting material on *Science* Online.
9. F. J. Wentz, *J. Geophys. Res.* **102**, 8703 (1997).
10. T. M. Smith, R. W. Reynolds, *J. Clim.* **18**, 2021 (2005).
11. Data are posted at www.ncdc.noaa.gov/oa/climate/research/ghcn/ghcngrid.html.
12. C. A. Mears, F. J. Wentz, *Science* **309**, 1548 (2005); published online 11 August 2005 (10.1126/science.1114772).
13. G. A. Meehl *et al.*, *Science* **307**, 1769 (2005).
14. R. F. Adler *et al.*, *J. Hydrometeorol.* **4**, 1147 (2003).
15. The satellite-gauge combined precipitation product V2 was downloaded from ftp://precip.gsfc.nasa.gov/pub/gpcp-v2/psg/.
16. J. P. Peixoto, A. H. Oort, in *Physics of Climate* (Springer, New York, 1992), pp. 170–172, 228–237.
17. W. D. Collins *et al.*, *NCAR Technical Note TN-464+STR* (National Center for Atmospheric Research, Boulder, CO, 2004).
18. J. W. Hurrell, Y. Kushnir, G. Ottersen, M. Visbeck, Eds., *The North Atlantic Oscillation: Climate Significance and Environmental Impact* (Geophysical Monograph Series, American Geophysical Union, Washington, DC, 2003), pp. 1–35.
19. W. L. Gates *et al.*, *Bull. Am. Meteorol. Soc.* **73**, 1962 (1998).
20. The more recent AMIP-II simulations were obtained from www-pcmdi.llnl.gov/projects/amip.
21. B. J. Soden, *J. Clim.* **13**, 538 (2000).

22. This work was supported by NASA's Earth Science Division.

Supporting Online Material

www.sciencemag.org/cgi/content/full/1140746/DC1
Materials and Methods
SOM Text
Fig. S1
References

2 February 2007; accepted 21 May 2007
Published online 31 May 2007;
10.1126/science.1140746
Include this information when citing this paper.

Supporting Online Material for

How Much More Rain Will Global Warming Bring?

Frank J. Wentz,* Lucrezia Ricciardulli, Kyle Hilburn, Carl Mears

*To whom correspondence should be addressed. E-mail: frank.wentz@remss.com

Published 31 May 2007 on *Science* Express
DOI: 10.1126/science.1140746

This PDF file includes:

Supporting Online Material: Materials and Methods

1. Computation of evaporation over the ocean

We compute evaporation over the oceans using the bulk formula from the NCAR Community Atmospheric Model 3.0 (S1). The rate of evaporation is proportional to the vertical gradient of specific humidity at the Earth's surface, which can be expressed by the bulk aerodynamic method:

$$E = \frac{\kappa\sqrt{\rho\tau_0}\,(q_0 - q_z)}{\ln\frac{z}{z_0} - \psi} \tag{S1}$$

where κ is von Karman's constant, ρ is the surface air density, τ_0 is surface wind stress, q_0 and q_z are the specific humidities at the surface and at height z. The terms z_0 and ψ are the roughness length and profile for latent heat flux. One advantage of using satellite wind retrievals as opposed to *in situ* wind measurements is that the satellite retrievals are a direct measurement of surface stress. Given τ_0, the bulk formulation simplifies in that the momentum drag coefficient is not needed. The specific humidities q_0 and q_z are functions of the sea-surface temperature (SST), the air temperature at height z, and the relative humidity (RH) at height z. These three terms come from ancillary datasets.

For SST we use the Reynolds' optimum interpolated product (OISST), which is derived from satellite infrared SST retrievals that are calibrated to *in situ* SST observations (S2). The marine air temperature (MAT) dataset comes from the Hadley Center (S3). The MATs are a quality-controlled global dataset of ship and buoy air temperature measurements, averaged over a 5° monthly grid. During the SSM/I period, the reference height for these air temperature measurements is z = 15 m. Only nighttime measurements are used to avoid biases due to solar heating of the ship decks.

We find that from 1987-2006 the MATs are cooling by 0.06 K decade^{-1} relative to the SST. This relative cooling trend in the MAT dataset has been noted elsewhere (S4) and was used to support early results from the satellite microwave sounding unit (MSU). This earlier version of MSU observations indicated the tropical lower troposphere (TLT) was not warming as much as the surface. However, an error in the methodology applied to the MSU was later found (S5), and the new results indicate the TLT is in fact warming faster than the surface as predicted by most climate models.

Given these new MSU results, it is difficult to explain the relative cooling trend in the MAT. Furthermore, if the cooling trend were real, the corresponding reduction in static stability would increase E by an additional 0.6% decade^{-1} to a value near 2% decade^{-1}. We do not consider such a large increase in evaporation as plausible. It is not consistent with the precipitation results and it is way out of line with climate model predictions (S6). Therefore, the relative cooling in the MAT is assumed to be a spurious artifact and is not incorporated it into our analysis. Rather, we average the difference ΔT = MAT - SST over 19 years and make climatology maps of ΔT at a 2.5° spatial resolution for each of the 12 months.

For RH we use the International Comprehensive Ocean-Atmosphere Data Set (ICOADS) (S7). We made trend maps of the ICOADS relative humidities and found no appreciable trends

that are above the noise level. This is in agreement with climate models, which in general predict little change in RH with global warming (S6, S8). The assumption of constant RH is also supported by *in situ* observations (S9) and satellite observations (S10). We treat the ICOADS dataset the same as the MAT dataset: we average over the 19 years and make 12 monthly climatology maps of RH.

2. Evaporation over land and ice

The estimation of evaporation over land is a difficult problem. Satellite estimates of τ_0 are not available, and other parameters such as soil moisture and land cover come into play. Fortunately for our analysis the contribution of land to global evaporation is only 14%, and we expect the contribution of land to the long-term variability of E to be small, albeit it is a source of error. We use a constant value of 527 mm yr^{-1} for all the continents excluding Antarctic (S11). Any actual trends in land evaporation would be a source of error in our results. For example the Global Precipitation Climatology Project (GPCP) (S12) precipitation values just over land for the 1987-2006 period show an increase of 14 mm yr^{-1} $decade^{-1}$. This might suggest an accompanying increase in evaporation over land due to more available surface water and soil moisture. If we were to assume E=P over land rather than using a static value for E, the global evaporation trend would increase from 1.3 % $decade^{-1}$ to 1.7 % $decade^{-1}$, giving us an even larger discrepancy with the climate model predictions. On the other hand, pan evaporation measurements possibly show a decrease in land evaporation, but the interpretation of these results is far from settled (S13). In any event, trends in the evaporation over land may have a small effect on our results, but it is unlikely that it will be large enough to change the basic conclusions of the study.

For Antarctica and sea ice we use a value of 28 mm yr^{-1} (S11). SSM/I measures the varying extent of the sea ice, and our method does accounts for the decline in the arctic sea ice. However the effect of declining sea ice on global evaporation is very small, being about +0.02% $decade^{-1}$.

Supporting Online Material: Text

1. SSM/I background

The Special Sensor Microwave Imager (SSM/I) is provided by the U.S. Defense Meteorological Satellite Program (DMSP). DMSP typically maintains two to three polar orbiting satellites in operation at any give time. The DMSP F08 satellite, which was launched in June 1987, flew the first SSM/I, and since then, five additional SSM/Is have been launched, with the last three still in operation as of the end of 2006. The SSM/I views the Earth in the spectral region from 19 to 85 GHz. The spectral and polarimetric information in this band is sufficient to retrieve a number of important geophysical parameters. Particularly accurate retrievals can be done over the world's oceans because a water surface provides a radiometrically cold background with a precisely known spectral and polarimetric signature. The over-ocean SSM/I retrievals include: surface wind stress, total atmospheric water vapor and cloud water, surface rain rate, and sea-ice extent (S14).

Realizing the potential importance of SSM/I observations to climate research, Remote Sensing Systems (RSS) early on initiated rigorous quality control procedures and advanced sensor calibration techniques to convert the SSM/I operational weather products into research-quality climate products (S15). Much of the early evidence of the decline in the Arctic sea ice extent came from analyses of these SSM/I observations (S16). Another important SSM/I finding was the close coupling between tropospheric warming and moistening (S10). This was revealed by comparing the decadal timeseries of SSM/I water vapor with the lower tropospheric temperatures coming from another series of satellite sensors: the microwave sounding unit (MSU).

The methods for retrieving precipitation (P), water vapor (V), and surface stress (τ_0) from the SSM/I microwave radiances are quite different. Precipitation retrievals are based on observing a spectral signature in the radiances that increases with frequency. The water vapor retrieval relies on the 22-GHz channel, which is centered on a weak water vapor absorption line. The retrieval of τ_0 is based on the depolarization of the surface emission due to the wind roughening of the sea surface. Although the three retrievals come from the same satellite sensor, their error characteristics can be considered independent because they respond very differently to errors in the radiance measurements.

2. Calibration of SSM/I radiances

The calibration of the SSM/I radiances has been an on-going project at RSS, and recently the 6th generation of SSM/I products was released (S17). The earlier versions of SSM/I retrievals were sufficiently accurate for monitoring the sea-ice extent and atmospheric water vapor because these two retrievals are relatively robust, requiring calibration accuracies at the 0.2 K level. However some of the other retrievals like wind speed are more sensitive to calibration errors. With this in mind, one of the primary objectives in the implementation of SSM/I Version 6 (V6) is to provide the community with a climate-quality wind speed dataset. In addition to a better calibration of the radiances, improved retrieval algorithms are implemented in V6. The algorithm improvements are particularly beneficial for the rain rate retrieval.

The calibration method for V6 closely follows that used for the intercalibration of the MSUs (S18). Like the MSUs, some of the SSM/Is exhibit errors that are correlated with the hot-load target temperatures, and we remove these errors using the MSU "target factor" approach (S18). The target-factor method was also used for SSM/I Version 5 (V5), but there were two problems. First, the V5 target factors for the F14 SSM/I were derived from the first 3 years of observations during which there was little variability in the hot-load temperature. Subsequently, the orbit for F14 drifted, its hot load began to experience very large swings in temperature, and the V5 target factors over-compensated for this change in temperature. For V6, we rederived the target factors using all of the F14 observations and verified that the new values worked appropriately for the entire F14 time period.

The second problem related to the F10 target factors. When the F10 observations are compared with simultaneous observations from other SSM/Is, a relatively large error becomes apparent. The error varies like a cosine function with a period of one year. In V5, we attempted to remove this error using the target factor method, which resulted in suspiciously large target factors. Subsequent analysis indicated that the correlation of the F10 error with the hot-load temperature (which also varied annually as a cosine) was coincidental. The true cause of the error is related to attitude anomalies in the F10 spacecraft. The launch of F10 was not completely successful, and the eccentricity of its orbit was large. This resulted in a relatively large variation in the Earth incidence angle over an orbit. In V6, the F10 error is modeled as an error in the reported incidence angle rather than an error related to the hot-load temperature.

A number of other refinements were implemented with V6 including using 10^{o} zonal intersatellite offsets rather than a single value. The V6 calibration also benefits from using a longer time period (1987-2006) as compared to V5 (1987-2001). The V6 ocean products are now freely available at www.remss.com.

3. Validation of the SSM/I winds and estimation of error bars

To validate the V6 SSM/I wind speeds, comparisons are made with ocean buoys and satellite scatterometer wind retrievals. The buoy measurements come from three networks of moored ocean buoys. The first two networks are the Tropical Atmosphere-Ocean (TAO/TRITON) network in the equatorial Pacific and the Pilot Research Moored Array in the Tropical Atlantic (PIRATA), both operated by NOAA's Pacific Marine Environmental Laboratory (PMEL) (S19, S20). The US National Data Buoy Center (NDBC) operates the third network, which consists of buoys in coastal regions around the continental United States, Alaska and Hawaii (S21). Care must be taken when doing the buoy validation. Due to their particular location with respect to ocean currents, upwelling area, atmospheric stability, and wind fetch, each buoy has a unique wind speed bias relative to the satellite retrieval of wind stress. This wind bias must be removed before doing the long-term stability validation or else buoys at new locations coming on-line and buoys at old locations going off-line will corrupt the analysis.

The two satellite scatterometers used in the validation are the ones that flew on the first European Remote Sensing satellite (ERS-1) (1992-1996) and on NASA's QuikScat satellite (1999-present) (S22, S23). The scatterometer wind retrievals are particularly useful in that one expects scatterometers to be less prone to calibration drifts than radiometers. The scatterometer wind retrieval is based on the ratio of received power to transmitted power, and this ratio should be insensitive to instrument drift.

The satellite wind retrievals are actually a measurement of surface stress τ_0. It is convenient to express τ_0 in terms of an equivalent neutral stability wind speed W at 10 m elevation (S11):

$$W = \frac{1}{C_D}\sqrt{\frac{\tau_0}{\rho}} \tag{S2}$$

where C_D = 0.0013 is the drag coefficient for neutral stability and ρ is the surface air density. The buoy wind measurements are also converted to a 10-m neutral stability wind using the air-sea temperature difference provided by the buoy. A ±1-hour and ±50-km collocation window is used to select those buoy observations that correspond to SSM/I overpasses.

To do the wind comparisons, monthly averages are first found and then the seasonal variability is removed, thereby producing monthly wind anomalies for SSM/I, the buoys, and the two scatterometers. The correlation between the monthly anomalies of SSM/I winds and buoys winds is 0.90, and the difference of the SSM/I trend minus the buoy trend is –0.02 m s^{-1} $decade^{-1}$. An error bar is assigned to the SSM/I wind trend by assuming the monthly SSM/I minus buoy wind speed difference ΔW is entirely due to errors in the SSM/I wind retrieval. The error ΔW has a standard deviation of 0.12 m s^{-1} and a lag-1 (i.e., 1 month) temporal autocorrelation r_1 of 0.46. This temporal correlation has the effect of reducing the effective sample size n_{eff} (i.e., the degrees of freedom) and results in the estimated trend error being larger than that coming from the simple least-squares method, which assumes each observation is independent. The effective sample size is given by (S24)

$$n_{eff} = n\frac{1-r_1}{1+r_1} \tag{S3}$$

where n is the number of months in the time series. This gives a trend error of ±0.05 m s^{-1} $decade^{-1}$ at the 95% confidence level. Essentially the same error bar is found by doing Monte Carlo simulations of a lag-1 autocorrelation timeseries.

Fig. S1 shows timeseries of the SSM/I, buoy, and scatterometer winds. To generate these timeseries, the monthly anomalies are low-pass filtered by convolution with a Gaussian distribution having a ±4-month width at half-peak power. Although the overall trend difference between SSM/I and the buoys is very small, the SSM/I-buoy wind speed difference ΔW shows features similar to the SSM/I-scatterometer ΔW. We apply a small empirical adjustment to the SSM/I winds to bring them into agreement with the buoy winds. This adjustment is simply a table of 20 numbers that correspond to the SSM/I-buoy ΔW for each year. The magnitude of these annual adjustments is about 0.1 m/s or less, and they have no effect on the overall trend. Fig. S1 shows that bringing the SSM/I into agreement with the buoys also improve the agreement with the scatterometers. The trend difference of the adjusted SSM/I wind minus the ERS-1 scatterometer and QuikScat is +0.03 m s^{-1} $decade^{-1}$ (same for both scatterometers). These adjusted winds are used in our report.

4. The sensitivity of evaporation to changes in surface temperature

The Clausius-Clapeyron (C-C) relationship specifies how saturation vapor pressure varies with temperature. The typically quoted C-C rate of 6.5% K^{-1} corresponds to a temperature of 15°C. For warmer temperatures the C-C rate is less. For example, the C-C rate is 5.8% K^{-1} for a typical surface temperature of 28°C over the tropical oceans. Since most evaporation occurs over the tropics, the effective C-C rate for evaporation tends to the tropical value. Also the air density ρ term in the bulk formula for evaporation varies inversely with temperature and tends to decrease the E versus temperature derivative. To model these effects, we used Eq. S1 to compute an average evaporation over the world's oceans assuming a realistic SST field. The calculation is then repeated adding 1°C to the SST field, and the evaporation increases by 5.7%. Thus we consider 5.7% K^{-1} as a typical rate for evaporation.

5. Using Version 6 over-ocean precipitation retrievals as compared to GPCP

To characterize the variability of rain over the ocean for the last two decades, we use our V6 SSM/I precipitation retrievals rather than the GPCP values. We have more confidence in the long-term calibration of V6 rain retrievals as opposed to the GPCP, which is a blend of retrievals from different types of satellites. As a test case, we repeated our analysis using the GPCP rain over the ocean rather than the V6 retrievals. Similar results were obtained, but the correlation between E and P was not as high. The E versus P correlation dropped from 0.68 to 0.57, and the global trend for P was 1.1% $decade^{-1}$ as compared to 1.4% $decade^{-1}$ for the standard analysis.

Although we have more confidence in the temporal variability of the V6 SSM/I rain product, the GPCP product has undergone extensive validation and probably is more accurate in an absolute sense. Accordingly, we adjusted the V6 rain rates to agree with the GPCP values in an absolute sense. This adjustment increased the V6 rain rates by 18% with most of the adjustment occurring in the middle latitudes. There is no time component to this adjustment and hence it does not affect temporal statistics given in the report.

6. Estimating an error bar for the precipitation and evaporation trends

When averaged globally over monthly time scales, precipitation and evaporation must balance except for a negligibly small storage term. This E=P constraint provides us with an error estimate for our derived values of E and P. The standard deviation of the monthly E-P values is 2.2%, and we assume the errors in E and in P contributed equally to E-P difference. The lag-1 (i.e., 1 month) temporal autocorrelation r_1 of E-P is 0.22. Following the method described above for assigning an error bar to the wind trend (S24), we find the trend error in precipitation and evaporation to be ± 0.5 % at the 95% confidence level.

7. Response of atmospheric general circulation to global warming

The response of general atmospheric circulation to global warming is a complex process that is yet to be resolved. The weakening of the equator-to-pole temperature gradient, which is predicted by most models, suggests a weakening of winds. However, other factors are also important. The Walker Circulation responds to east-west temperature gradients (S25). If the

continents warm more than the ocean, this will affect winds. Mesoscale convection may increase in the tropics due to warmer sea surface temperatures. Small changes in the tropical lapse rate or atmospheric static stability could have a significant impact on circulation (S26). Satellite measurements of the thermal radiation emitted by the Earth suggest a strengthening of tropical general circulation during the 1985-2000 period (S27), and reanalyses indicate the Hadley cell has strengthened over the last several decades, contrary to the model predictions (S28). On the other hand, Indo-Pacific sea level pressure records from 1861 to present indicate a decrease in the Walker circulation, more in line with model predictions (S29).

Supporting Online Material: Figure

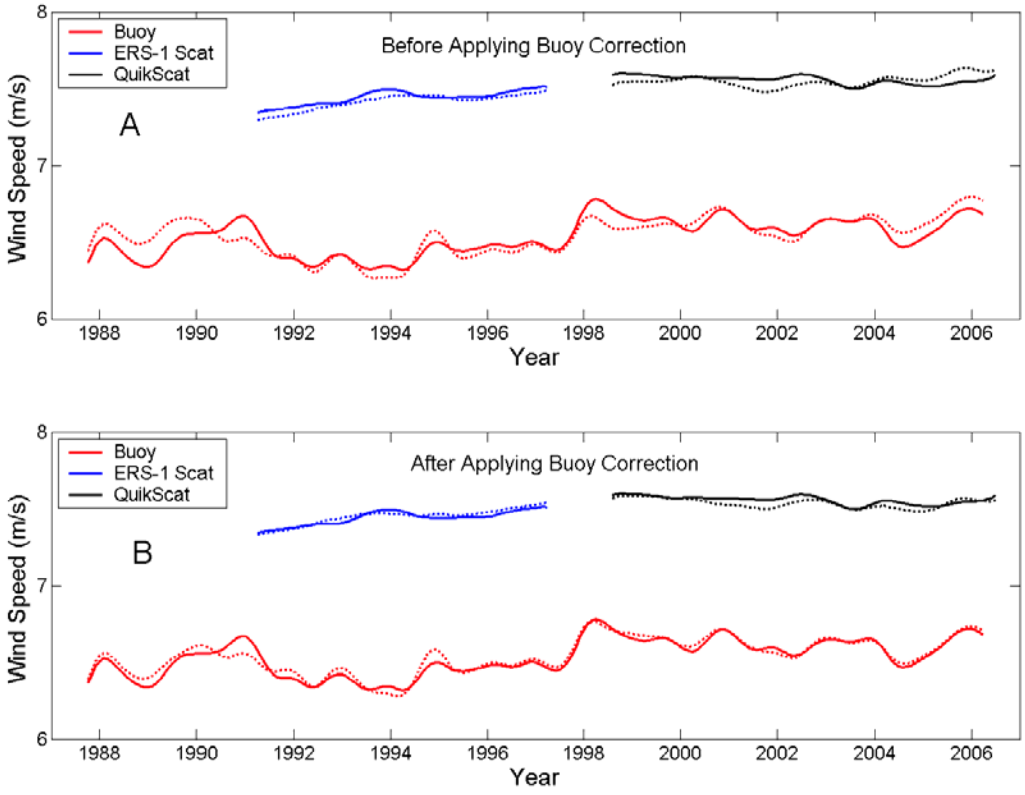

Fig. S1. A comparison of SSM/I wind retrievals with buoy winds and wind retrievals from satellite scatterometers. (A) The red curves show the results from collocated SSM/I and buoy observations. The solid line is the buoy wind and the dotted line is the collocated SSM/I wind. In producing the timeseries, the seasonal variability is removed and a ±4-month smoothing window is applied. Similar comparisons of the SSM/I collocated with the ERS-1 scatterometer and the QuikScat scatterometer are shown by the blue and black curves, respectively. The solid lines are the scatterometer winds and the dotted lines are the SSM/I winds. (B) Same as (A) except that a small correction has been applied to the SSM/I winds to match the buoy winds on a yearly basis. Note that this correction also improves the agreement of SSM/I with the scatterometers. The average wind speed for the buoy collocations is lower than that for the scatterometer collocations because many of the buoys are in the tropics where winds are generally lower than the global mean value of 7.5 m s^{-1}.

Supporting Online Material: References and Notes

S1. W. D. Collins *et al.*, "Description of the NCAR Community Atmosphere Model (CAM 3.0)", *NCAR Technical Note*, NCAR/TN-464+STR (2004).

S2. R. W. Reynolds, N. A. Rayner, T. M. Smith, D. C. Stokes, W. Wang, *J. Climate*, **15**, 1609 (2002).

S3. N. A. Rayner *et al., J. Geophys. Res*, **108**, 10.1029/2002JD002670 (2003). We used the MOHMAT43N dataset downloaded from http://www.hadobs.org.

S4. J. R. Christy *et al*., *Geophys. Res. Lett.*, **28**, 183 (2001).

S5. C. A. Mears, F. J. Wentz, *Science*, **309**, 1548 (2005); published online 11 August 2005 (10.1126/science.1114772).

S6. J. F. B. Mitchell, C. A. Wilson, W. M. Cunnington, *Q. J. R. Meteorol. Soc*., **113**, 293 (1987).

S7. S. J. Worley, S. D. Woodruff, R. W. Reynolds, S. J. Lubker, N. Lott, *Int. J. Climatol.*, **25**, 823, 10.1002/joc.1166 (2005). The marine monthly summaries of the enhanced (ships+buoys) ICOADS 2.3 dataset downloaded from http://dss.ucar.edu/pub/coads.

S8. M. R. Allen, W. J. Ingram, *Nature*, **419**, 224 (2002).

S9. P. Peixoto, A. H. Oort, *J. Climate*, **9**, 3443 (1996).

S10. F. J. Wentz, M. Schabel, *Nature*, **403**, 414 (2000).

S11. J. P. Peixoto, A. H. Oort, *Physics of Climate*, (Springer-Verlag, New York, 1992), pp. 170-172, 228-237.

S12. R. F. Adler *et al*., *J. Hydrometeor*., **4**,1147 (2003).

S13. A. Ohmura, M. Wild, *Science*, 298, 1345 (2002).

S14. F. J. Wentz, *J. Geophys. Res*., **102**, 8703 (1997).

S15. F. J. Wentz, "User's manual SSM/I antenna temperature tapes", *RSS Technical Report 120191* (1991).

S16. D. J. Cavalieri, P. Gloersen, C. L. Parkinson, H. J. Zwally, J. C. Comiso, *Science*, **278**, 1104 (1997).

S17. SSM/I V6 products are at http://www.ssmi.com/ssmi/ssmi_description.html.

S18. C. A. Mears, M. Schabel, F. J. Wentz, *J. Climate*, **16**, 3650 (2003).

S19. M. J. McPhaden, *Bull. Am. Met. Soc*., **76**, 739 (1995).

S20. J. Servain *et al.*, *Bull. Am. Met. Soc.*, **79**, 2019 (1998).

S21. D. Gilhousen, *J. Atm. Ocean. Tech*., **4**, 94 (1987).

S22. E. Attema, *Proceedings of the IEEE*, **79**, 791 (1991).

S23. M. W. Spencer, C. Wu, D. G. Long, *IEEE Trans. Geosci. Remote Sens*., **38**, 89 (2000).

S24. B. D. Santer *et al*., *Science*, 287, 1227 (2000).

S25. M. L. Salby, *Fundamentals of Atmospheric Physics*, (Academic Press, New York, 1996), pp. 50-52.

S26. C. M. Mitas, A. Clement, *Geophys. Res. Lett.*, **33**, L01810 (2006).

S27. J. Chen, B. E. Carlson, A. D. Del Genio, *Science*, **295**, 838 (2002),

S28. C. M. Mitas, A. Clement, *Geophys. Res. Lett.*, **32**, L03809 (2005).

S29. G. A. Vecchi *et al*., *Nature*, **44**, 73 (2006).